IRAQI JOURNAL OF MATERIALS
Volume (5) Issue (2) April-June 2026, pp. 67-76
Published and Sponsored by American Quality for Scientific Publishing, Inc. (AQSP)

Electrical and Optical Characteristics of Heterostructures Fabricated From Porous Silicon Structures Decorated with $NiCo_2O_4$ Nanoparticles by Solution Casting Method

Farah M. Wanas, Jasim K. Yasin*, Ohood J. Kadhum

Department of Physics, College of Science, University of Thi Qar, Nasiriyah, IRAQ
** Corresponding author email: jasimyaseen2019@gmail.com*

Abstract
In this work, Nickel cobaltite ($NiCo_2O_4$) nanoparticles were incorporated into a porous silicon (PSi) structures prepared on silicon substrates by photoelectrochemical etching (PECE) technique. The electrical characteristics of the fabricated photodetector showed that the heterojunction of $NiCo_2O_4$ nanoparticles concentration of $4x10^{-4}$ M exhibits higher photocurrent than the heterojunction of concentration of $4x10^{-4}$ M. The optoelectronic characteristics showed that the photodetector fabricated with $NiCo_2O_4$ concentration of $4x10^{-4}$ M is better than that with concentration of $4x10^{-4}$ M. The optimum photodetector showed a responsivity of 1.22 A/W, an external quantum efficiency of 2.32, and a detectivity of 14.37×10^{10} Jones. The response of the fabricated photodetectors was evaluated as a function of time and found dependent on the concentration (and hence layer thickness) of the $NiCo_2O_4$ nanoparticles as the device fabricated with lower concentration (smaller thickness) showed faster response.

Keywords: Nickel cobaltite; Porous silicon; Heterostructures; Solution casting method
Received: November 2025; **Revised:** January 2026; **Accepted:** February 2026; **Published:** April 2026

1. Introduction

The hybrid heterojunction detectors are a qualitative revolution in optoelectronics and sensing techniques as they are based on the combination of the characteristics of inorganic and organic semiconductors at the nanoscale to create new functions not available in the individual components [1-4]. Semiconducting nanoparticles or quantum dots represent the fundamental component of the hybrid heterojunction detectors due to their unique optical and electronic characteristics governed by the quantum mechanics, mainly the quantum confinement effect, that allows controlling the energy bandgap and hence the absorption and emission wavelengths by controlling the particle size [5,6]. Such characteristics give these nanoparticles high sensitivity to light as well as high efficiency to generate electron-hole pairs when illuminated with radiation. However, the largest challenge is how to incorporate these nanoparticles in a functional structure allowing the collection of generated charges and transfer them efficiently to the electrodes [7-9]. Here, the role of porous silicon can be observed as an ideal platform for incorporation and hybridization.

Porous silicon is usually prepared by the electrochemical etching of a single-crystalline silicon wafer in hydrofluoric (HF) acid solutions. This etching results in the formation of a porous structure with drastically high internal surface area that its porosity and dimensions can be precisely controlled by the variation of some preparation parameters such as current density, etching time, solution concentration, and illumination intensity [10-13]. The prepared porous structure show excellent optical characteristics including its ability to trap light and multiple reflections within the pores to support the absorption of the incident photons. Furthermore, porous silicon shows additional feature throughout the photoluminescence in the visible region as a result of silicon nanostructure quantization [14-16].

Typically, fabrication techniques of hybrid heterojunction detectors include two main steps. First, preparation of semiconducting nanoparticles by wet chemical methods such as thermal decomposition or chemical bath deposition to ensure uniform size distribution and high crystallinity. Second, doping or decoration of porous silicon with these nanoparticles, which can be carried out by infiltration from colloidal solutions depending on capillarity feature of the pores, or by synchronized electrochemical deposition that allows the preparation of the nanoparticles inside the pore with single step [17-22]. The incorporation process can produce hybrid heterojunctions at the interface between nanoparticles (usually of wide energy bandgap) and porous silicon (indirect bandgap semiconductor). This generates

an internal electric field supporting charge separation and preventing recombination, and hence enhancing the photoconversion efficiency [23-25]. The applications of these detectors widely extend to include high-sensitive gas sensors at room temperature as the structural characteristics of the heterojunctions as well as the large surface area of porous silicon lead to reasonable variation in the electrical characteristics upon the absorption of gas molecules [26,27]. Also, these heterojunctions play pivotal role in developing hybrid solar cells by the combination of nanoparticles absorption efficiency and stability and low cost of silicon, to exceed the limits of conventional solar cells [28]. Moreover, the hybrid heterojunction detectors are used in bioimaging and biosensors due to their biocompatibility and ability of surface morphology to link the biomolecules [29]. They are also used in the UV detectors due to their high sensitivity and fast response [30]. The continuous developments in nanomaterial synthesis techniques can provide more enhancement in the performance of such hybrid detectors and make them promising candidates for the next generation of multifunction integrated optoelectronic devices.

The hybrid structures based on the incorporation of semiconducting ferrite or cobaltite nanoparticles – with unique optical and electrical characteristics – in porous silicon structures are reasonably promising for the applications of photodetectors and optoelectronic devices. These characteristics are originated from the synergetic effects resulted from the combination of the two nanoscale materials [31-33]. Optically, the porous silicon – as a porosity-controlled medium – participates to support light absorption via trapping and multi-directional scattering within the porous structure. This supports the ability of the ferrite or cobaltite nanoparticles to absorb light over a wide spectral range due to their semiconducting nature and relative narrow energy bandgap to extend the spectral responsivity of the photodetectors fabricated from these hybrid structures [34-36]. Furthermore, the possibility of enhanced magneto-optic effects to occur in such nanocomposites can induce some advanced applications to control light by magnetic fields [37-39].

In this work, nickel cobaltite nanomaterial was used to fabricate heterojunctions with a porous silicon layer formed on a silicon substrate formed by the photoelectrochemical etching (PECE) method. The optoelectronic properties of these heterojunctions were determined and analyzed.

2. Experimental Work

In order to prepare the porous silicon region on a p-type silicon substrate by the photoelectrochemical etching (PECE), as shown schematically in Fig. (1), the silicon substrate was cut into 2.54x2.54 cm square samples. These samples were thoroughly cleaned with ethanol and distilled water, then kept in HF: ethanol (1:10) solution for 10 minutes. Then the sample was washed with deionized water and kept in methanol. It was placed inside the PECE cell, which contains (1:1) HF:ethanol solution for 10 minutes with 30 mA current and irradiated with a laser beam of 650 nm wavelength. After completing the process, the sample was kept in methanol to prevent the oxidation and contamination from the surrounding environment.

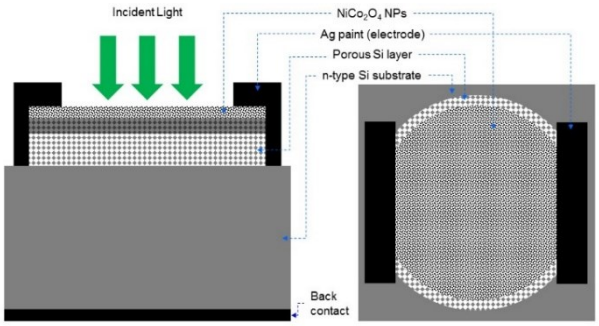

Fig. (1) Schematic diagram of the $NiCo_2O_4$NPs/PSi/Si structure fabricated in this work

A 10cm-diameter 99.9% purity $NiCo_2O_4$ target supplied by ALB Materials (USA) was sputtered to deposit $NiCo_2O_4$ thin films on glass substrates using DC plasma sputtering technique. The aqueous solutions of $NiCo_2O_4$ nanoparticles were prepared by dispersing specific weight (1 mg and 10 mg) of the $NiCo_2O_4$ nanoparticles in 10 mL of deionized distilled water to form two different concentrations ($4x10^{-4}$ M and $4x10^{-3}$ M, respectively). The prepared solution was sonicated for 15 minutes and then 100 µL was taken and manually dropped on the porous silicon layer formed on the silicon substrate. The sample

 ISSN (print) 2958-8960 (online) 3006-6042 Printed in IRAQ

was left on the hotplate at 40°C for 30 seconds before dropping the next droplet. Aluminum contacts were deposited on the back side of the silicon substrate whereas silver paint was used to form the front electrode on the substrate's surface.

The structural and morphological characteristics of the prepared samples were investigated using X-ray diffraction (XRD) patterns, field-emission scanning electron microscopy (FE-SEM), atomic force microscopy (AFM), and Fourier-transform infrared (FTIR) spectrometry. The absorption spectra of the fabricated samples were recorded using a UV-visible spectrophotometry in the spectral range of 200-1000 nm. The electrical characteristics of the fabricated heterojunctions were determined using a DC power supply and an accurate ammeter with a halogen lamp as a radiation source for illumination measurements.

3. Results and Discussion

Figure (2) shows the XRD patterns of the PSi layer, $NiCo_2O_4$ nanoparticles, and $NiCo_2O_4$ NPs/PSi structure prepared in this work. The XRD pattern of $NiCo_2O_4$ NPs shows a polycrystalline structure with five distinct peaks at 31.55°, 35.93°, 39.03°, 63.16°, and 68.44°, which correspond to the crystalline planes of (220), (311), (222), (511), and (440) planes, respectively. Indeed, these peaks are attributed to inverted spinel type according to JCPDS card 20-0781 [40-42]. The XRD pattern of PSi exhibits three peaks located at 28°, 47°, and 69.2°, corresponding to (111), (220), and (400) planes, respectively. The XRD pattern of $NiCo_2O_4$ NPs-decorated PSi shows the presence of peaks belonging to $NiCo_2O_4$ NPs and PSi (400). The intensities of two peaks of PSi at 28° and 47° were reasonably suppressed due to the incorporation of $NiCo_2O_4$ NPs inside the pores. As shown in the XRD pattern, no peaks belonging to other materials than $NiCo_2O_4$ and PSi were observed.

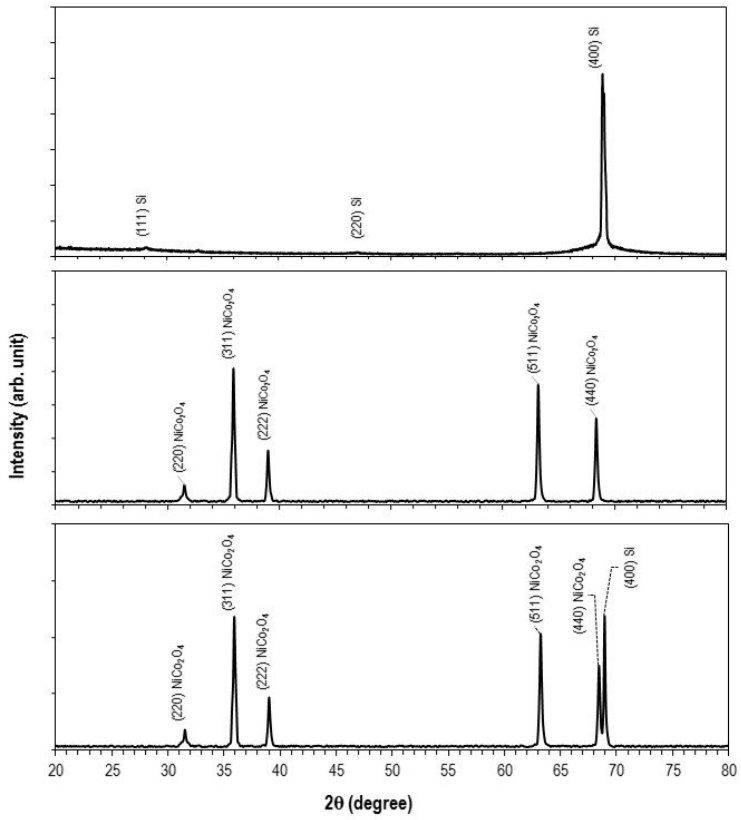

Fig. (2) XRD patterns of PSi (upper), $NiCo_2O_4$ NPs (middle), and $NiCo_2O_4$ NPs/PSi structure (lower) prepared in this work

Figure (3a) shows the FE-SEM images of the porous silicon (PSi) region formed on the silicon substrate by the PECE method. The image confirms the successful formation of a porous structure, with an average pore size of approximately 375 nm. These pores are uniformly distributed across the entire

 ISSN (print) 2958-8960 (online) 3006-6042 Printed in IRAQ

IRAQI JOURNAL OF MATERIALS
Volume (5) Issue (2) April-June 2026, pp. 67-76
Published and Sponsored by American Quality for Scientific Publishing, Inc. (AQSP)

silicon surface, and the porosity is estimated to be 75%. Such a high porosity is beneficial for applications requiring high surface area, such as sensor devices and photodetectors. The thickness of porous silicon layer was determined from the cross-sectional FE-SEM image (Fig. 3b) to be 13-17 µm, which may reveal the uniform formation of pores on the surface of silicon substrate. Figure (5c) presents the FE-SEM image of $NiCo_2O_4$ nanoparticles (NPs) decorating the PSi surface. The nanoparticles have penetrated the pores, with some also deposited on the walls between the pores (Fig. 4d). This occurs because the $NiCo_2O_4$ NPs, with a minimum particle size of 10 nm, are significantly smaller than the pore size, allowing multiple particles to occupy a single pore. The image also reveals areas where agglomeration of nanoparticles has occurred, resulting in larger clusters of $NiCo_2O_4$ NPs. These larger agglomerates sometimes appear to obstruct or partially fill the pores.

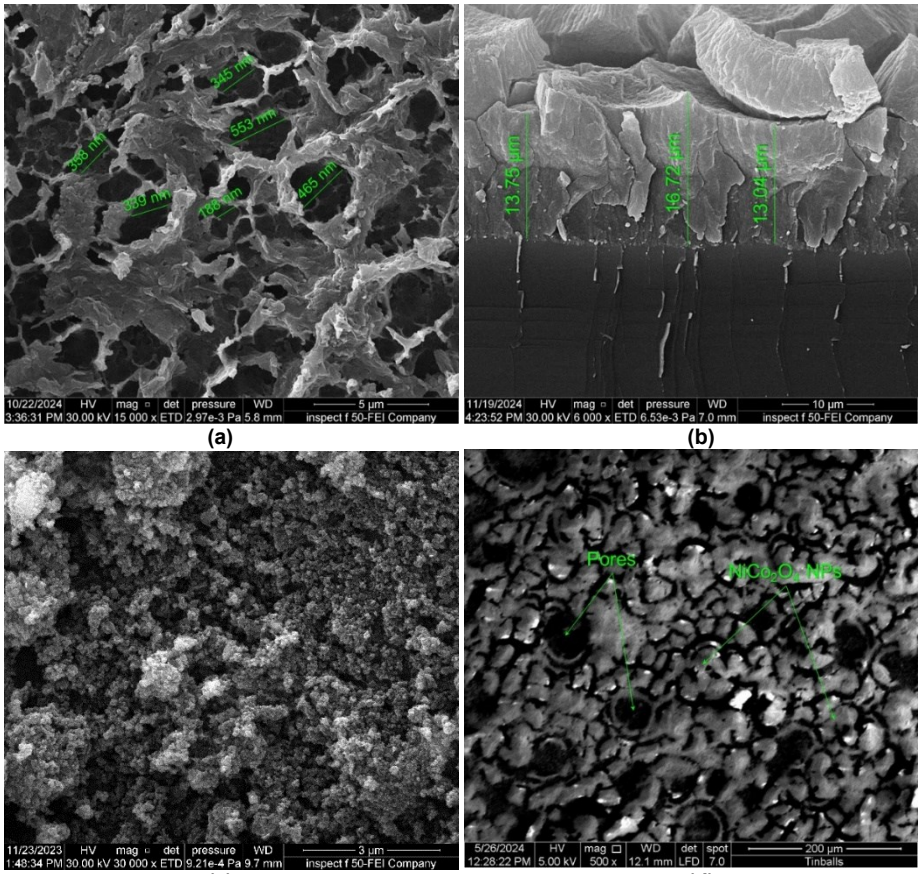

Fig. (3) FE-SEM images of (a) porous silicon layer, (b) cross-sectional porous silicon layer, (c) $CoFe_2O_4$ NPs, and (d) $CoFe_2O_4$ NPs deposited on porous silicon layer

The non-uniform distribution of $NiCo_2O_4$ NPs across the PSi surface is attributed to the manual drop casting method used during deposition. Although this method allows for nanoparticle infiltration into the pores, it also results in areas where the agglomeration occurs, which could affect the uniformity and potentially impact the device performance. Despite this, the $NiCo_2O_4$ NPs effectively cover the entire porous surface, indicating that the pores are sufficiently filled with nanoparticles, providing a favorable interface for applications like photodetection or gas sensing. It is important to note that the agglomeration of $NiCo_2O_4$ NPs could influence the overall properties of the device, including optical absorption, charge transport, and sensitivity in sensor applications. The presence of isolated nanoparticles and agglomerates might create heterogeneous active sites, which could enhance or limit performance depending on the specific application. However, the embedded nanoparticles and agglomerates contribute to increased surface area and provide an opportunity for the formation of $CoFe_2O_4$/PSi hybrid structures, which can be explored for various practical applications.

Figure (4) shows the dark forward and reverse current-voltage characteristics of $CoFe_2O_4$ NPs-decorated PSi heterojunction measured in the voltage range of -4 to +4 V. The two heterojunctions

IRAQI JOURNAL OF MATERIALS
Volume (5) Issue (2) April-June 2026, pp. 67-76
Published and Sponsored by American Quality for Scientific Publishing, Inc. (AQSP)

exhibit rectifying properties. The forward current of these junctions increases with bias voltage according to the diode equation. In the first region (low voltage region), the current increases slightly with voltage due to the recombination, while the second region shows that the current increases exponentially with bias voltage due to the domination of diffusion current over the recombination current. The forward current of the heterojunction with $CoFe_2O_4$ concentration of $4x10^{-4}$ M is larger than that of concentration of $4x10^{-3}$ M due to the lower electrical resistivity of the $CoFe_2O_4$ film. The reverse current increases slightly with reverse voltage for two heterojunctions. The ideality factor (n) of the heterojunctions was determined using the following diode equation [43]:

$$I = I_0\left(e^{\frac{qV}{nk_BT}} - 1\right) \quad (1)$$

where I_0 is the saturation current, q is the electron charge, k_B is the Boltzmann coefficient, and T is the operating temperature. After using Eq. (1), the ideality factor for heterojunction prepared at $CoFe_2O_4$ concentrations of $4x10^{-4}$ M and $4x10^{-3}$ M was 1.61 and 5.02, respectively. These values are sufficiently larger than the typical range (1-2), which is attributed to the increase in the saturation current as a result of the porous structure. The turn-on voltage of the heterojunctions prepared at concentrations of $4x10^{-4}$ M and $4x10^{-3}$ M, as shown in Fig. (4), was 1.8 and 3 V, respectively. The large value of the turn-on voltage of the heterojunction prepared at a nanoparticles concentration of $4x10^{-3}$ M is attributed to the high electrical resistivity of the film. The turn-on voltage of the heterojunction prepared with a $CoFe_2O_4$ nanoparticles concentration of $4x10^{-3}$ M is larger than that of the heterojunction with a nanoparticles concentration of $4x10^{-4}$ M. This can be ascribed to the higher electrical resistivity of $CoFe_2O_4$. In $CoFe_2O_4$ layers with larger concentration, the electrical resistivity tends to dominate, leading to a higher potential barrier that requires a larger voltage to make the current flow. Moreover, $CoFe_2O_4$ layers with larger concentration frequently exhibit less favorable charge transport properties due to reduced carrier mobility and increased scattering at the interfaces. On the other hand, a $CoFe_2O_4$ layer with a lower concentration may facilitate better charge conduction due to the reduced effect of interfacial defects and scattering, causing a lower turn-on voltage.

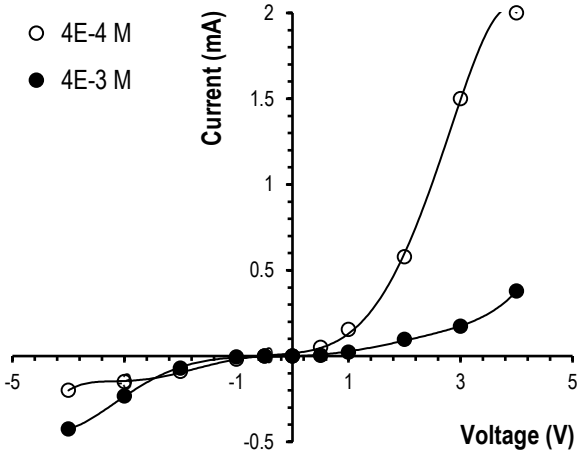

Fig. (4) I-V characteristics of heterojunctions fabricated with $NiCo_2O_4$ NPs concentrations of $4x10^{-4}$ M and $4x10^{-3}$ M

The illuminated I-V characteristics of $CoFe_2O_4$ NPs-decorated PSi heterojunction photodetectors are shown in Fig. (5). While the photodetector is illuminated with light, an electron-hole pair generated in the depletion region and contributes to increasing the current of the photodetector. The presence of an internal electric field at the depletion region prevents any possible electron-hole recombination. The increase in the light intensity results in an increase in the photocurrent of the photodetector. No significant saturation in photocurrent was observed after increasing the light intensity to 135 mW/cm^2.

The photocurrent of the photodetector prepared with a nanoparticles concentration of $4x10^{-4}$ M is larger than that of nanoparticles concentration of $4x10^{-3}$ M. This result is due to the nanoparticles agglomeration with large $CoFe_2O_4$ layer thickness. As layer thickness is increased, the tendency of $CoFe_2O_4$ nanoparticles to agglomerate becomes more pronounced, resulting in larger clusters and reduced surface area. Actually, the agglomeration of the $CoFe_2O_4$ nanoparticles can hinder effective light absorption and reduce the photogenerated carriers [44]. In addition, agglomeration can create defects and increase scattering at the grain boundaries, both of which can degrade charge transport.

While, in the case of a thinner $CoFe_2O_4$ layer likely has a more uniform nanoparticle distribution, optimizing light absorption and minimizing recombination sites, thereby enhancing photocurrent generation. It can be concluded that controlling the morphology and particle dispersion is important in optimizing the performance of $CoFe_2O_4$-based photodetectors. The photocurrent was increased as bias voltage increased due to the increase in the width of the depletion region. The photosensitivity plot of the photodetectors as a function of bias voltage is shown in Fig. (6). The photosensitivity of the photodetector prepared at the nanoparticles concentration of $4x10^{-3}$ M is higher than that of nanoparticles concentration of $4x10^{-4}$ M. This result can be attributed to the high absorption occurring in $CoFe_2O_4$ film as well as, due to the agglomeration of the grains on the pores of porous silicon [45].

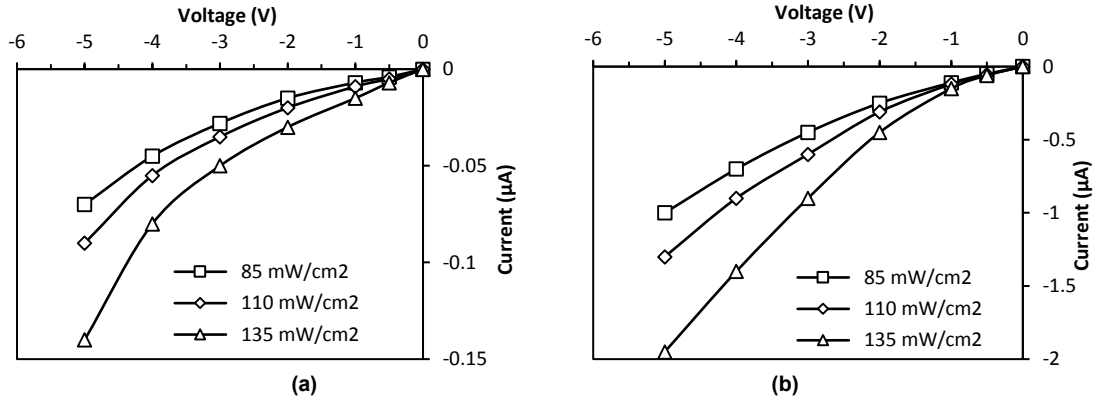

Fig. (5) I-V characteristics under illumination conditions of the heterojunctions fabricated with $NiCo_2O_4$ NPs concentration of (a) $4x10^{-4}$ M, and (b) $4x10^{-3}$ M

On the other hand, the maximum photosensitivity was found at the bias voltage of 5 V. Increasing photosensitivity with bias voltage arising from an increase in the dark current. Figure (7) shows the spectral responsivity (R_λ) of $CoFe_2O_4$ NPs-decorated PSi heterojunction photodetectors fabricated using two nanoparticles concentrations of $4x10^{-4}$ M and $4x10^{-3}$ M at two bias voltages of 5 and 10 V. The responsivity of the photodetector prepared at nanoparticles concentration of $4x10^{-4}$ M shows the maximum responsivity of 1.22 A/W at 650 nm and 5 V biasing voltage due to the absorption edge of $CoFe_2O_4$ film.

The short wavelengths are absorbed in the film surface and the wavelengths are longer than the cut-off wavelength of $CoFe_2O_4$ film absorbed in PSi and Si substrate. The responsivity at the wavelength range of 500-700 nm comes from the light absorbed in PSi layer, while the wavelength longer than 700 nm is absorbed in the Si substrate. An increase in the bias voltage from 5 to 10 V results in an increase in the responsivity of the photodetector due to widening the depletion region and increasing the electric field. No effect of bias voltage on the position of the peak response was observed.

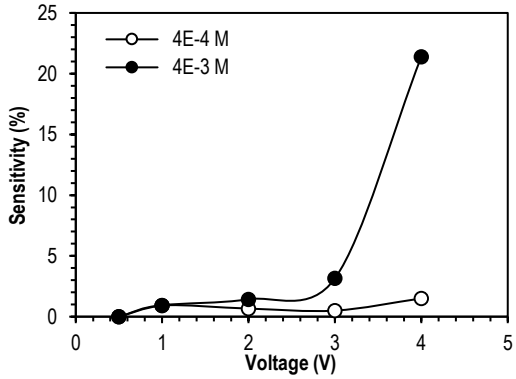

Fig. (6) Photosensitivity versus bias voltage of the $NiCo_2O_4$ NPs-decorated PSi photodetectors fabricated with two nanoparticles concentrations ($4x10^{-4}$ M and $4x10^{-3}$ M)

IRAQI JOURNAL OF MATERIALS
Volume (5) Issue (2) April-June 2026, pp. 67-76
Published and Sponsored by American Quality for Scientific Publishing, Inc. (AQSP)

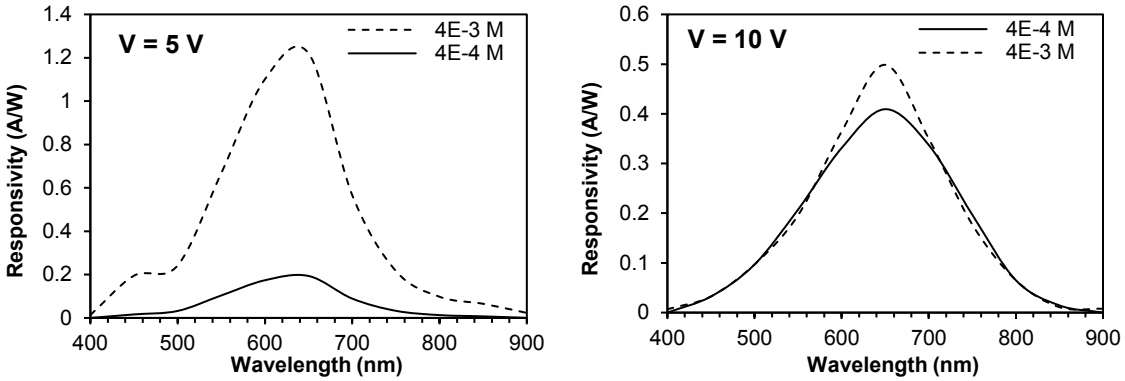

Fig. (7) Spectral responsivity plot of $NiCo_2O_4$ NPs-decorated PSi photodetectors fabricated with two nanoparticles concentrations of $4x10^{-4}$ M and $4x10^{-3}$ M, and at 5 V and 10 V biasing voltage

The external quantum efficiency EQE of the photodetector was calculated using the following relationship [43]:

$$EQE = \frac{1250\, R_\lambda}{\lambda\ (nm)} \qquad (2)$$

Figure (8) shows the effect of bias voltage and $CoFe_2O_4$ layer thickness on the external quantum efficiency (EQE) of the photodetectors. As shown, the maximum EQE value of 2.32% was achieved for the heterojunction with a $CoFe_2O_4$ nanoparticles concentration of $4x10^{-4}$ M at a wavelength of 650 nm and a biasing voltage of 5 V. In contrast, for the heterojunction with $CoFe_2O_4$ nanoparticles concentration of $4x10^{-3}$ M, the EQE dropped to 0.369% at the same wavelength (650 nm). This difference is attributed to the higher collection efficiency of photogenerated carriers in the thinner $CoFe_2O_4$ layer. The thinner $CoFe_2O_4$ layer allows more photons to penetrate deeper into the porous silicon substrate, where the majority of electron-hole pair photogeneration occurs. Thicker $CoFe_2O_4$ layers, however, tend to absorb more light before it reach the silicon, reducing the number of photons available for carrier generation. In addition, with a thinner $CoFe_2O_4$ layer, photogenerated carriers have a shorter distance to travel before reaching the depletion region, which minimizes recombination losses and enhances charge collection, thereby increasing the EQE. On the contrary, in the case of the thicker $CoFe_2O_4$ layer (nanoparticles concentration of $4x10^{-3}$ M), photon absorption predominantly occurs within the $CoFe_2O_4$ itself, limiting the number of photons reaching the silicon substrate. Additionally, the longer distance that photogenerated carriers must travel to reach the depletion region increases the likelihood of recombination, further decreasing the EQE.

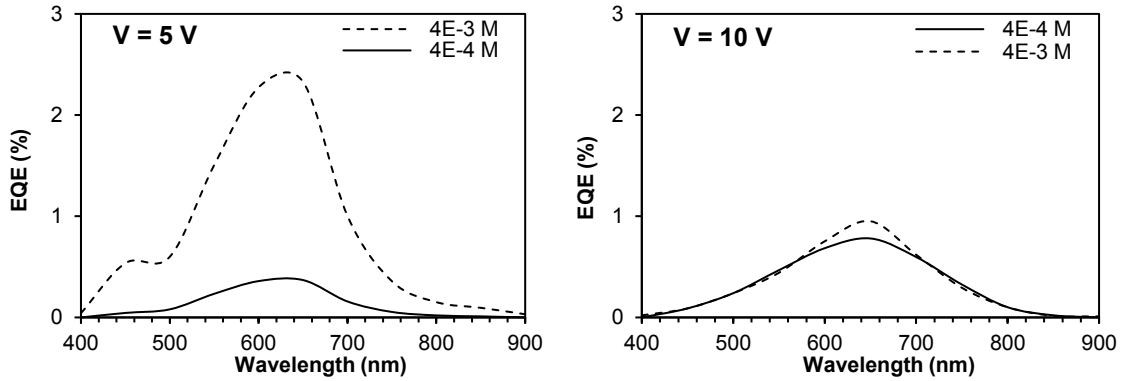

Fig. (8) Variation of the EQE of the heterojunctions fabricated with two different $NiCo_2O_4$ NPs concentrations ($4x10^{-4}$ M and $4x10^{-3}$ M) and two different biasing voltages (5 V and 10 V)

Figure (9) shows the specific detectivity (D^*) of the heterojunction photodetectors fabricated with two different thicknesses of the $CoFe_2O_4$ NPs layer and two different biasing voltages. The specific detectivity is one of the important parameters of the photodetector, which describes the ability of the photodetector to detect the light signal. The specific detectivity can be estimated using the following equation [43]:

$$D^* = R_\lambda \sqrt{\frac{A}{2qI_{dark}}} \quad (3)$$

where I_d is the dark current at a certain bias voltage, and A represents the photosensitive area of the photodetector. The behavior of detectivity (D^*) is observed to follow a trend similar to that of spectral responsivity and external quantum efficiency. As the biasing voltage increases from 5 to 10 V, the detectivity (D^*) increases, and this increase is higher for the device fabricated with a larger thickness of $CoFe_2O_4$ NPs layer. This enhancement is attributed to the increased responsivity resulting from the widening of the depletion layer width at higher bias voltages, which improves carrier separation and reduces recombination losses. Consequently, more photo-generated carriers are collected, leading to higher detectivity.

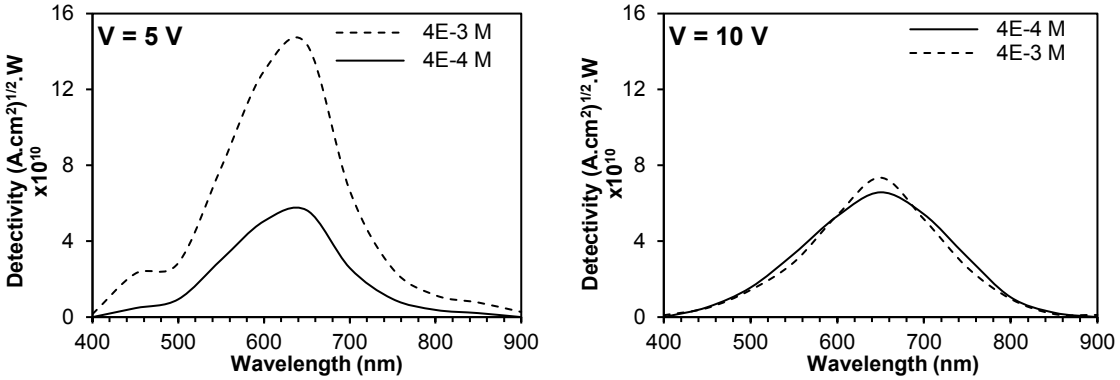

Fig. (9) Variation of the specific detectivity (D^*) of the heterojunctions fabricated with two different $NiCo_2O_4$ NPs concentrations ($4x10^{-3}$ M and $4x10^{-3}$ M) and two different biasing voltages (5 V and 10 V)

The noise equivalent power (NEP) of the photodetector was found to be dependent on the thickness of the $CoFe_2O_4$ NPs layer as well as on biasing voltage as shown in Fig. (10). A smaller NEP means that the photodetector has a better ability to detect weak signals. Therefore, the heterojunction photodetectors fabricated using lower concentrations of $CoFe_2O_4$ NPs and operated at a lower biasing voltage (3 V) show smaller NEP than the higher concentrations and biasing voltages.

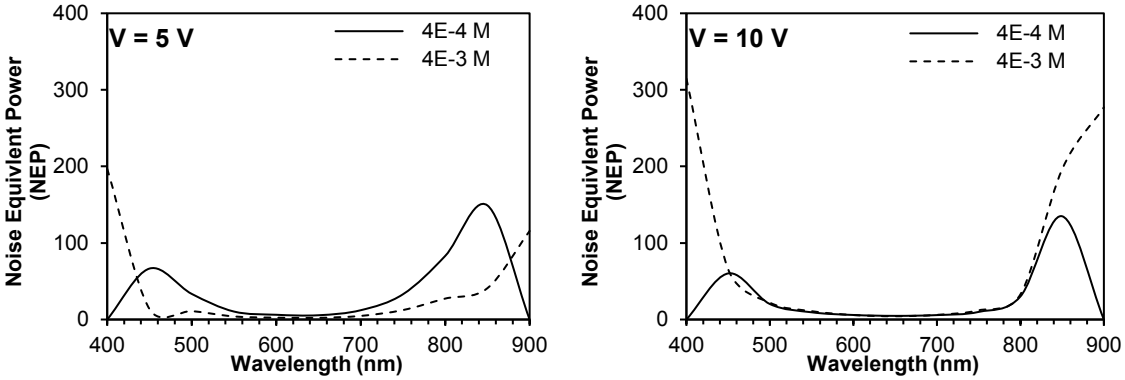

Fig. (10) Variation of the NEP of the heterojunctions fabricated with two different $NiCo_2O_4$ NPs concentrations ($4x10^{-3}$ M and $4x10^{-3}$ M) and two different biasing voltages (5 V and 10 V)

The photodynamic response time is the most important parameter considered to determine how fast the photodetector response. Figure (12) shows the effect of $CoFe_2O_4$ nanoparticles concentration (and hence layer thickness) on the photodynamic response time of the photodetectors based on the fabricated heterojunctions. The ratio of rise time to fall time for the photodetectors fabricated with $CoFe_2O_4$ nanoparticles concentrations of $4x10^{-4}$ M and $4x10^{-3}$ M were 0.82 and 0.89, respectively, at a bias voltage of -5 V. This indicates a slightly faster response with decreasing layer thickness, which could be attributed to the changes in charge carrier dynamics. The reduced rise and fall times for the thinner $CoFe_2O_4$ layer suggest that the photogenerated carriers experience more efficient transport and recombination due to the decreased absorption and enhanced carrier mobility in the thinner layer [46]. The ON/OFF ratio (ON refers to illuminated state and OFF is the dark state) signifies the contrast

between the photocurrent and dark current and was also determined.

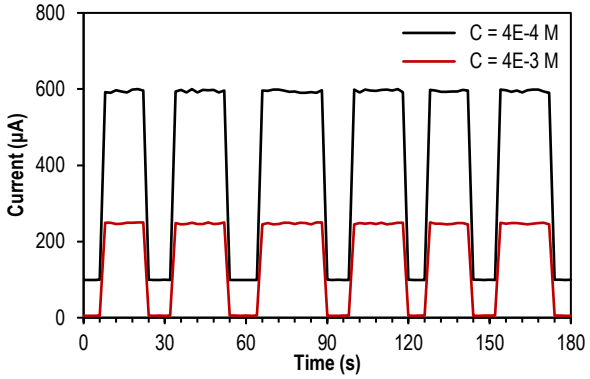

Fig. (10) Real-time photodynamic response of the photodetectors fabricated with nanoparticles concentrations of 4x10^{-4} M and 4x10^{-3} M, respectively (photocurrent response under on/off light illumination)

4. Conclusion

In this study, porous silicon (PSi) layer was formed on the silicon surface by the photoelectrochemical etching (PECE) method to fabricate $NiCo_2O_4$NPs/PSi heterojunctions. The $NiCo_2O_4$ nanoparticles were embedded within the pores of the PSi layer, effectively decorating the surface. The fabricated heterojunctions exhibited rectifying behavior, with the I-V characteristics aligning with the recombination-tunneling model. The photodetector fabricated with a $NiCo_2O_4$ nanoparticles concentration of 4x10^{-3} M and biasing voltage of 5 V demonstrated superior photosensitivity compared to other devices fabricated with a larger thickness of this layer. The optimum photodetector showed a responsivity of 1.22 A/W, an external quantum efficiency (EQE) of 2.32, and a detectivity (D^*) of 14.37×10^{10} Jones.

References

[1] J.A.R. Ramón et al., "Inducing Superparamagnetism and High Magnetization in Nickel Cobaltite ($Ni_xCo_{3-x}O_4$) Spinel Nanoparticles by Controlling Ni Mole Fraction and Cation Distribution", *The J. Phys. Chem. C*, 124 (2020) 18264-18274.
[2] B. Sachin Kumar et al., "Graphene nanoclusters embedded nickel cobaltite nanofibers as multifunctional electrocatalyst for glucose sensing and water-splitting applications", *Ceram. Int.*, 45(18) (2019) 25078-25091.
[3] N. Cárdenas et al., "Synthesis and characterization of nickel cobaltite–supported film for hexavalent chromium photocatalytic reduction", *Water Sci. Technol.*, 90(7) (2024) 2131-2145.
[4] S. Divya, T.H. Oh, and M. Bodaghi, "1D nanomaterial based piezoelectric nanogenerators for self-powered biocompatible energy harvesters", *Euro. Polym. J.*, 197 (2023) 112363.
[5] A. Fatoni et al., "Glucose biosensor based on activated carbon – $NiFe_2O_4$ nanoparticles composite modified carbon paste electrode", *Result Chem.*, 4 (2022) 100433.
[6] E.A. Alghamdi and R. Sai, "Adjusting the gas detection characteristics of $NiFe_2O_4$ spinel ferrite nanoparticles through the introduction of Zn doping", *Result Phys.*, 59 (2024) 107549.
[7] S.S. Vadla et al., "Electrodeposited $NiFe_2O_4/Cu_2O$ heterostructure thin films with enhanced photocurrent generation", *J. Photochem. Photobiol.*, 15 (2023) 100181.
[8] R. Verma et al., "Nanoengineered parallelogram-$NiFe_2O_4$/rGO nanocomposite-based biosensing interface for highly efficient electrochemical detection of neurodegenerative disorders via dopamine monitoring", *RSC Appl. Interfaces*, 1(2) (2024) 252-267.
[9] A.R. Malik et al., "Lime peel extract induced $NiFe_2O_4$ NPs: Synthesis to applications and oxidative stress mechanism for anticancer, antibiotic activity", *J. Saudi Chem. Soc.*, 26(2) (2022) 101422.
[10] S. tul Shafa et al., "Synthesis and characterization of Cu and Tb substituted $NiFe_2O_4$@MXene nanocomposite as a new photocatalyst for removal of organic dyes and drugs from industrial wastewater", *Result Phys.*, 63 (2024) 107844.
[11] R. Devi et al., "Au/$NiFe_2O_4$ nanoparticle-decorated graphene oxide nanosheets for electrochemical immunosensing of amyloid beta peptide", *Nanoscale Adv.*, 2(1) (2020) 239-248.
[12] B. Godbole et al., "Synthesis, Structural, Electrical and Magnetic Studies of Ni- Ferrite Nanoparticles", *Phys. Procedia*, 49 (2013) 58-66.
[13] S. Tufail et al., "2D nanostructures: Potential in diagnosis and treatment of Alzheimer's disease", *Biomed. Pharmacother.*, 170 (2024) 116070.
[14] E.M. Kamar, M. Khairy, and M.A. Mousa, "Effect of morphology and particle size on the electrical properties of nano-nickel ferrite", *J. Mater. Res. Technol.*, 24 (2023) 7381-7393.
[15] A. Toghan et al., "Effect of particle size and morphological structure on the physical properties of $NiFe_2O_4$ for supercapacitor application", *J. Mater. Res. Technol.*, 19 (2022) 3521-3535.
[16] Priyanka et al., "Biosynthesis, characterization and enhanced photocatalytic and antibacterial activity of Paspalidium flavidum mediated ZnO nanoparticles", *Desalin. Water Treat.*, 123 (2018) 300-308.
[17] E. Aslan et al., "Enhancing performance of SnS_2 based self-powered photodetector and photocatalyst by Na incorporation", *Ceram. Int.*, 50(15) (2024) 27626-27634.
[18] F.J. Kadem, B.T. Chead and U.A. Yaseen, "Characteristics of Nickel Ferrite Nanostructures Prepared by DC Reactive

Magnetron Co-Sputtering", *Iraqi J. Sci. Indust. Res.*, 3(4) (2024) 19-22.
[19] F.J. Kadhim and R.A. Mohammed, "Structural Characteristics of Nickel Ferrite Nanoparticles Synthesized by New Arrangement of Concentric Targets in DC Reactive Magnetron Sputtering", *Iraqi J. Appl. Phys.*, 12(4) (2016) 9-12.
[20] J. Haman, "New Geometrical Arrangement to Prepare Nickel Ferrite Nanostructures on Glass Substrates Using DC Reactive Magnetron Sputtering", *Iraqi J. Sci. Indust. Res.*,, 3(2) (2024) 42-46.
[21] Majumder et al., "Anisotropy, Magnetostriction and Converse Magnetoelectric Effect in Dy Substituted Ni Ferrite", *Phys. Procedia*, 75 (2015) 238-244.
[22] R. Kurosawa et al., "Variations in the saturation magnetization of nanosized $NiFe_2O_4$ particles on adsorption of carboxylic acids", *J. Asian Ceram. Soc.*, 2(1) (2014) 41-43.
[23] J.L. Domínguez-Arvizu et al., "Study of $NiFe_2O_4/Cu_2O$ p-n heterojunctions for hydrogen production by photocatalytic water splitting with visible light", *J. Mater. Res. Technol.*, 21 (2022) 4184-4199.
[24] F. Shateran, M.A. Ghasemzadeh, and S.S. Aghaei, "Preparation of $NiFe_2O_4$@MIL-101(Fe)/GO as a novel nanocarrier and investigation of its antimicrobial properties", *RSC Adv.*, 12(12) (2022) 7092-7102.
[25] A.D. Khalaji, "$NiFe_2O_4$ prepared by the chitosan-assisted route for the photodegradation of methylene blue under simulated sun light irradiation", *Chem. Phys. Impact*, 8 (2024) 100652.
[26] S. Kamal et al., "Synthesis of boron doped $C_3N_4/NiFe_2O_4$ nanocomposite: An enhanced visible light photocatalyst for the degradation of methylene blue", *Result. Phys.*, 12 (2019) 1238-1244.
[27] M. Moradi-Bieranvand et al., "Construction of magnetic $MoS_2/NiFe_2O_4$/MIL-101(Fe) hybrid nanostructures for separation of dyes and antibiotics from aqueous media", *RSC Adv.*, 14(16) (2024) 11037-11056.
[28] B.T.P. Quynh et al., "Magnetic $NiFe_2O_4$ decorated-exfoliated graphite for adsorptive removal of anionic dyes and cationic dyes from aqueous solution", *Desalin. Water Treat.*, 82 (2017) 101-113.
[29] N.V. Thang, N.H. van Dijk, and E. Brück, "Effects of Milling Conditions on Nano-scale MnFe(P,Si) Particles by Surfactant-assisted High-energy Ball Milling", *Phys. Procedia*, 75 (2015) 1104-1111.
[30] E. Pérez, G. Marquez and V. Sagredo, "Effect of Calcination on Characteristics of Nickel Ferrite Nanoparticles Synthesized by Sol-Gel Method", *Iraqi J. Appl. Phys.*, 15(1) (2019) 13-17.
[31] S. Baul et al., "Investigation of the structural, magnetic and dielectric properties of $NiFe_2O_4$/nanoclay composites synthesized via sol-gel autocombustion", *J. Mater. Res. Technol.*, 27 (2023) 6606-6618.
[32] E. Sarala et al., "Green synthesis of nickel ferrite nanoparticles using Terminalia catappa: Structural, magnetic and anticancer studies against MCF-7 cell lines", *J. Hazard. Mater. Adv.*, 8 (2022) 100150.
[33] H. Wang et al., "One-pot solvothermal preparation of MFe_2O_4 (M=Ca, Mg and Ni) ferrite- graphene oxide nanocomposites for adsorption of acridine orange", *Desalin. Water Treat.*, 298 (2023) 174-183.
[34] G. Patel et al., "Direct one-pot synthesis of imines/benzothiazoles/benzoxazoles from nitroarenes via sequential hydrogenation-condensation using Nano-$NiFe_2O_4$ as catalyst under microwave irradiation", *Curr. Res. Green Sustain. Chem.*, 4 (2021) 100149.
[35] A.J. Raheem and S.M. Raji, "Nickel Ferrite Nanostructures Prepared by DC Reactive Magnetron Sputtering", *Iraqi J. Appl. Phys. Lett.*, 7(2) (2024) 7-10.
[36] R. Tiwari et al., "Structural and magnetic properties of tailored $NiFe_2O_4$ nanostructures synthesized using auto-combustion method", *Result Phys.*, 16 (2020) 102916.
[37] T.L. Lambat et al., "Recent developments in the organic synthesis using nano-$NiFe_2O_4$ as reusable catalyst: A comprehensive synthetic & catalytic reusability protocol", *Result Chem.*, 6 (2023) 101176.
[38] T. Shanmugavel et al., "Tailoring the Structural and Magnetic Properties and of Nickel Ferrite by Auto Combustion Method", *Procedia Mater. Sci.*, 6 (2014) 1725-1730.
[39] M.A. Shilpa Amulya et al., "Sonochemical synthesis of $NiFe_2O_4$ nanoparticles: Characterization and their photocatalytic and electrochemical applications", *Appl. Surf. Sci. Adv.*, 1 (2020) 100023.
[40] A. Safdar et al., "Biogenic synthesis of nickel cobaltite nanoparticles via a green route for enhancing the photocatalytic and electrochemical performances", *Sci. Rep.*, 14 (2024) 17620.
[41] M.A. Abduljabar and S.H. Merza, "Synthesis, Characterization of Nickel Cobaltite Nanoparticles and Its Use in Removal Methyl Green Dye from Aqueous Solution", *Ibn Al-Haitham J. Pure Appl. Sci.*, 37(3) (2024) 264-278.
[42] O.A. Hammadi and N.E. Naji, "Characterization of polycrystalline nickel cobaltite nanostructures prepared by DC plasma magnetron co-sputtering for gas sensing applications", *Photo. Sens.*, 8 (2018) 43-47.
[43] S.M. Sze and K.K. Ng, **"Physics of Semiconductor Devices"**, 3rd ed., Wiley-Interscience (NJ, 2007), p. 119, 618, 667, 125, 666.
[44] A.S. Hashim and B.K. Lateef, "Characteristics of Nickel Ferrite Thin Film Magnetic Sensor Fabricated by Sputtering Technique", *Iraqi J. Appl. Phys. Lett.*, 7(1) (2024) 7-10.
[45] K. Tang et al., "Enhancing UV photodetection performance of an individual ZnO microwire p-n homojunction via interfacial engineering", *Nanoscale*, 15(5) (2023) 2292-2304.
[46] P.C. Eng, S. Song, and B. Ping, "State-of-the-art photodetectors for optoelectronic integration at telecommunication wavelength", *Nanophoton.*, 4 (2015) 277-302.

 ISSN (print) 2958-8960 (online) 3006-6042 Printed in IRAQ